



Article

# Bismuth Nanoparticles Encapsulated in a Porous Carbon Skeleton as Stable Chloride-Storage Electrodes for Seawater Desalination

Xiaoqing Dong <sup>1</sup>, Ying Wang <sup>2</sup>, Qian Zou <sup>2</sup> and Chaolin Li <sup>2,\*</sup>

<sup>1</sup> Department of Environmental Engineering Technology, Shenzhen Institute of Information Technology, Shenzhen 518172, China

<sup>2</sup> School of Civil and Environmental Engineering, Harbin Institute of Technology (Shen Zhen), Shenzhen 518055, China; 20s054041@stu.hit.edu.cn (Y.W.); 22s154117@stu.hit.edu.cn (Q.Z.)

\* Correspondence: lichaolin@hit.edu.cn

**Abstract:** Cost-effective bismuth (Bi) boasts a high theoretical capacity and exceptional selectivity towards  $\text{Cl}^-$  ion storage, making it a promising material for desalination batteries (DBs). However, the substantial volume expansion and low conductivity severely hinder the cycling performance of Bi-based DBs. In this study, a carbon-layer-coated Bi nanocomposite (Bi@C) was synthesized by pyrolyzing a metal–organic framework (Bi-MOF) containing Bi using a straightforward method. The results show that the Bi@C synthesized under the condition of annealing at 700 °C for 2 h has the optimum properties. The Bi@C has good multiplication performance, and the desalination capacity is 106.1 mg/g at a high current density of 1000 mA/g. And the material exhibited a high desalination capacity of 141.9 mg/g at a current density of 500 mA/g and retained 66.9% of its capacity after 200 cycles. In addition, the Bi@C can operate at a wide range of NaCl concentrations from 0.05 to 2 mol/L. The desalination mechanism analysis of the Bi@C revealed that the carbon coating provides space for Bi particles to expand in volume, thereby mitigating the issues of electrode material powdering and shedding. Meanwhile, the porous carbon skeleton establishes electron and ion channels to enhance the electrode material’s conductivity. This research offers a promising strategy for the application of chloride-storage electrode materials in electrochemical desalination systems.



**Citation:** Dong, X.; Wang, Y.; Zou, Q.; Li, C. Bismuth Nanoparticles Encapsulated in a Porous Carbon Skeleton as Stable Chloride-Storage Electrodes for Seawater Desalination. *Batteries* **2024**, *10*, 35. <https://doi.org/10.3390/batteries10010035>

Academic Editor: Changshin Jo

Received: 9 December 2023

Revised: 11 January 2024

Accepted: 16 January 2024

Published: 19 January 2024



**Copyright:** © 2024 by the authors. Licensee MDPI, Basel, Switzerland. This article is an open access article distributed under the terms and conditions of the Creative Commons Attribution (CC BY) license (<https://creativecommons.org/licenses/by/4.0/>).

## 1. Introduction

With the increase in population and industrialization, the scarcity of freshwater resources has become an increasingly pressing issue globally [1,2]. Seawater, being abundant, readily available, and inexpensive, could significantly alleviate the water scarcity problem if effectively utilized [3]. Although advanced desalination technologies such as reverse osmosis (RO) [4] and multistage flash evaporation (MSF) [5] have been proposed to produce clean water, their widespread application is limited due to high energy consumption and secondary pollution concerns [6,7]. Consequently, novel green and low-energy desalination technologies have emerged [8–12]. Capacitive deionization (CDI) exhibits low energy consumption and environmental friendliness and has garnered widespread attention [13,14]. However, the traditional carbon-based capacitive deionization system only removes approximately 20 mg/g of salt [15] and is not suitable for highly concentrated seawater [16], thereby limiting its large-scale application in seawater desalination. Substituting the ion adsorption electrode with an ion-embedded electrode could effectively address this issue. Consequently, desalination batteries (DBs) with a high desalination capacity have been progressively drawing the attention of researchers.

Significant efforts have been devoted to exploring sodium-ion-storage electrode materials, but chloride-ion-storage electrodes have been comparatively less investigated. The

limited variety of available chloride-storage electrode materials and the dearth of extensive research on the chloride-storage mechanism have contributed to the slow development of chloride-storage electrodes [17]. Thanks to its high theoretical desalination capacity [18], silver is most widely used for chloride storage in desalination [19–22]. However, the high cost of silver and the low conductivity of AgCl continue to impede the application of Ag/AgCl electrodes in practical devices [20]. In recent years, bismuth and bismuth oxychloride (Bi/BiOCl) have been demonstrated to exhibit promising performances as alternative chloride-storage electrode materials. Han et al. [23] initially investigated the desalination efficiency of Bi and BiOCl electrodes, and paired the Bi electrode with NaTi<sub>2</sub>(PO<sub>4</sub>)<sub>3</sub> to construct a desalination cell. The results indicated that the Bi electrode possessed an initial desalination capacity of up to 129 mg/g. Chen et al. [24] introduced the concept of a portable bi-ionic electrochemical deionization technique, which employs BiOCl as the chloride Faraday negative electrode, boasting a stable and reversible desalination capacity of 68.5 mg/g. This is more than twice the previously reported optimal performance of 31.2 mg/g in the HCDI (Hybrid Capacitor Deionization) system. Despite the promising desalination performance of Bi/BiOCl, the capacity decay is too rapid due to the volume expansion (~158%) induced by the conversion of Bi to BiOCl, leading to the pulverization and shedding of the material. Furthermore, the low electrical conductivity of BiOCl limits the advancement of bismuth research [15,25].

Researchers and scholars have made many attempts to nanosize or dope Bi with carbon to improve the desalination capacity. For example, Nam et al. [26] prepared a Bi foam electrode with electrodeposition and paired it with Cu<sub>3</sub>[Fe(CN)<sub>6</sub>]<sub>2</sub>·nH<sub>2</sub>O. The Bi electrode has a high interfacial area, which is favorable for the diffusion of chloride ions into the Bi lattice, and the desalination capacity was maintained at 87.8% after 20 cycles of charge/discharge, with the shortcoming that in order to improve the reduction efficiency of BiOCl, the BiOCl reduction was carried out in a solution of hydrochloric acid of pH 1.2 during discharge, but this operation cannot be applied on a large scale in the practical industry. Liu et al. [27] prepared BiOCl-CNF by anchoring nano-BiOCl on electrospun carbon nanofibers for a rocking-chair capacitive deionization system, and by appropriately adjusting the composition of the hybrid materials, the BiOCl-CNF-based RCDI showed good results in the desalination capacity (124 mg/g), energy consumption (66.8 Wh/m<sup>3</sup>), power consumption (1.8 Wh/m<sup>3</sup>) (66.8 Wh/m<sup>3</sup>), and desalination rate (0.52 mg/g per second).

Analyzing the current reports, it can be observed that many systems do not charge and discharge in the same electrolyte in order to achieve good material recovery. After charging in neutral NaCl, BiOCl is separately placed in a hydrochloric acid solution for conversion during the reduction process [23,26,28], which avoids the problem of slow kinetics of BiOCl reduction and the inability to achieve complete reduction, but reduces the operability of bismuth application in desalination batteries. The development of bismuth chlorine-storage desalination batteries with excellent performance and feasible operation has become an urgent issue.

Here, we propose a constraint strategy to restrict the comminution of Bi nanoparticles during the DB process and effectively mitigate the problem of low conductivity of the Bi electrode. The prepared chlorine-storage electrode was based on the simple carbonization of the Bi-containing metal–organic framework (Bi-MOF), and Bi nanoparticles were uniformly covered in mesoporous carbon materials. Thanks to the stable carbon skeleton structure, the Bi@C maintained good stability during the reaction process, allowing for the volume expansion of the Bi chloride storage and discharge process. Additionally, the porous carbon skeleton provided electronic and ionic channels for enhanced electronic conductivity. As a result, the corresponding Faraday electrode showed excellent performance with a desalination capacity of up to 141.9 mg/g and a capacity retention of 66.9% after 200 cycles, which was superior to recent reports (Table S1).

## 2. Experimental Section

### 2.1. Materials and Chemicals

Bismuth nitrate pentahydrate ( $\text{Bi}(\text{NO}_3)_3 \cdot 5\text{H}_2\text{O}$ ), nitric acid ( $\text{HNO}_3$ ), and sodium chloride ( $\text{NaCl}$ ) were purchased from Aladdin Reagent Co. (Shanghai, China) Homobenzoic acid ( $\text{H}_3\text{BTC}$ ), methanol ( $\text{CH}_3\text{OH}$ ), and N,N-dimethylformamide (DMF) were purchased from McLean Reagents Ltd. (Changzhou, China) and N-methylpyrrolidone (NMP) and polyvinylidene difluoride (PVDF) were purchased from Arkema, Colombes, France.

### 2.2. Preparation of Materials

The first step was the preparation of Bi-MOF with the solvothermal method: specifically, 3.659 mmol of homobenzoic acid ( $\text{H}_3\text{BTC}$ ) and 0.309 mmol of  $\text{Bi}(\text{NO}_3)_3 \cdot 5\text{H}_2\text{O}$  were added to a mixture of N, N-dimethylformamide/methanol (60 mL, 4:1) at room temperature. After the powders were completely dissolved, the clear solution was transferred to a 100 mL PTFE-lined steel reactor. The reaction was heated to 120 °C in a sealed reactor for 24 h. The product was washed and cleaned with methanol three times and centrifuged to obtain a white powder, which was dried in a vacuum oven at 60 °C for 3 h. The dried white powder was ground and mixed.

The dried white powder was ground and transferred to a corundum boat placed in a tube furnace and heated to 600 °C, 700 °C, and 800 °C under an argon atmosphere, with the sintering time set to 4 h and the temperature increase rate to 5 °C/min. After the annealing was completed and the products were collected with the furnace cooled down to room temperature, the products were named Bi@C-600 °C, Bi@C-700 °C, and Bi@C-800 °C. In addition, the fixed sintering material temperature was 700 °C, and the sintering time was changed to 0.5, 1, 2, and 4 h. The corresponding products were named Bi@C-0.5 h, Bi@C-1 h, Bi@C-2 h, and Bi@C-4 h in turn.

### 2.3. Electrode Fabrication

The prepared active material was mixed with Super P in a mass ratio of 8:1 and ground in a mortar for 30 min, and the mixture obtained by mixing and grinding was added to a N-methylpyrrolidone binder dissolved in polyvinylidene fluoride and stirred for 6 h to obtain a slurry mixture. The mass ratio of poly(vinylidene fluoride) to Super P was 1:1, and the mass ratio of poly(vinylidene fluoride) to N-methylpyrrolidone was 1:19. The resulting slurry mixture was applied to the carbon paper and dried in a vacuum drying oven at 70 °C for 12 h to obtain the electrode sheet.

### 2.4. Material Characterization

The sample morphology was examined with scanning electron microscopy (SEM, ZEISS SUPRA® 55, Carl Zeiss, Jena, Germany) and X-ray diffraction pattern analysis (XRD, DX-27 mini). Nitrogen adsorption and desorption tests were carried out to obtain data on the specific surface area and pore size of the samples. An X-ray fluorescence spectroscopy test (XPS, Thermo Scientific K-Alpha, Waltham, MA, USA) was used to determine the composition of the material to be tested. A thermogravimetric analysis (TGA) was carried out at 900 °C in oxygen to determine the sample content.

### 2.5. Electrochemical Testing

The electrochemical properties of the materials were tested in a 0.6 M NaCl electrolyte using a three-electrode system. The electrodes were discharged prior to each performance test, reducing the oxidized state of the material to Bi. The electrode to be tested was fixed as a working electrode with a platinum sheet electrode holder. An activated carbon fiber felt with an area of 1.5 mm was fixed to the platinum sheet electrode holder as the counter electrode. The reference electrode was a saturated silver/silver chloride reference electrode (the potential difference between Ag/AgCl and NHE is 0.198 V). The electrochemical measurements were carried out on an electrochemical workstation (Correst, CS350H, Wuhan, China) with a three-electrode system, and cyclic voltammetry (CV), constant-

current charge/discharge (GCD), and electrochemical impedance spectroscopy (EIS) were sequentially conducted.

The electrode desalination capacity (IRC) was calculated as:

$$\text{IRC} = \frac{2.18 \times I \times t}{m} \quad (1)$$

where  $I$  is the current applied during desalination (milliamps),  $t$  is the electrode charging duration (hours), and  $m$  is the electrode mass (grams).

The Coulombic efficiency (CE) was calculated as:

$$\text{CE (\%)} = \frac{C_{i,d}}{C_{i,c}} \times 100 \quad (2)$$

where  $C_{i,d}$  and  $C_{i,c}$  are the specific capacities at discharge and charge in the  $i$ th cycle, respectively.

### 3. Results and Discussion

#### 3.1. Optimization of the Preparation Process of MOF-Derived Bismuth Carbon Materials

##### 3.1.1. Optimization of Sintering Temperature

During the annealing process, the high temperature causes the particles to intensify the collision and thus agglomerate together. However, too low of a temperature can lead to incomplete reactions and excessive impurities [3]. As can be seen from Figure 1d, the main diffraction peaks of Bi@C-600 °C, Bi@C-700 °C, and Bi@C-800 °C corresponded to the Bi standard card, with sharp peaks and good crystallinity, proving that the synthesized material was Bi metal. The diffraction peaks of the carbon were not found on the graph, so the carbon in the synthesized material was in an indeterminate form. The stray peaks located at the diffraction angles of 27.9, 32.7, and 55.5 degrees belonged to the Bi oxide that was not sufficiently reduced during the thermal reduction process. As can be seen from the SEM image, when the sintering temperature was 600 °C (Figure 1a), the Bi presented as concave spherical particles loaded on the carbon skeleton, which was mainly in the form of uneven columns with rough surfaces. When the sintering temperature reached 700 °C (Figure 1b), the Bi spheres had a smooth surface and were uniformly loaded on the carbon skeleton. The statistics of metal particle size at this temperature showed that the particle size was mainly distributed between 70 and 220 nm, with an average particle size of 148 nm. It is worth noting that the average particle size of Bi@C-700 °C was lower than that of Bi@C-600 °C. The reason was that the Bi-MOF structure was a columnar structure, and the temperature was low under the annealing condition of 600 °C, so the metal ions and the organics in the inner part of the columnar structure received less energy and the Bi was mostly reduced to Bi nanoparticles encapsulated in the carbon skeleton, which were not exposed in the visible range of the scanning electron microscope. And the metal ions and the organics outside the columnar structure absorbed most of the heat, reacted, and aggregated together without being restricted during the growth process. The external metal ions and organics absorbed most of the heat and reacted, and the Bi was not restricted in the growth process and aggregated together. When the annealing temperature reached 700 °C, the organic columnar structure of the precursor unfolded in the form of a flower due to the growth of Bi spheres inside, with sufficient energy and uniform Bi growth. When the annealing temperature reached 800 °C, as shown in (Figure 1c), the Bi spheres were heavily aggregated and seriously separated from the carbon skeleton, and the size of the Bi clumps reached more than 20 μm.

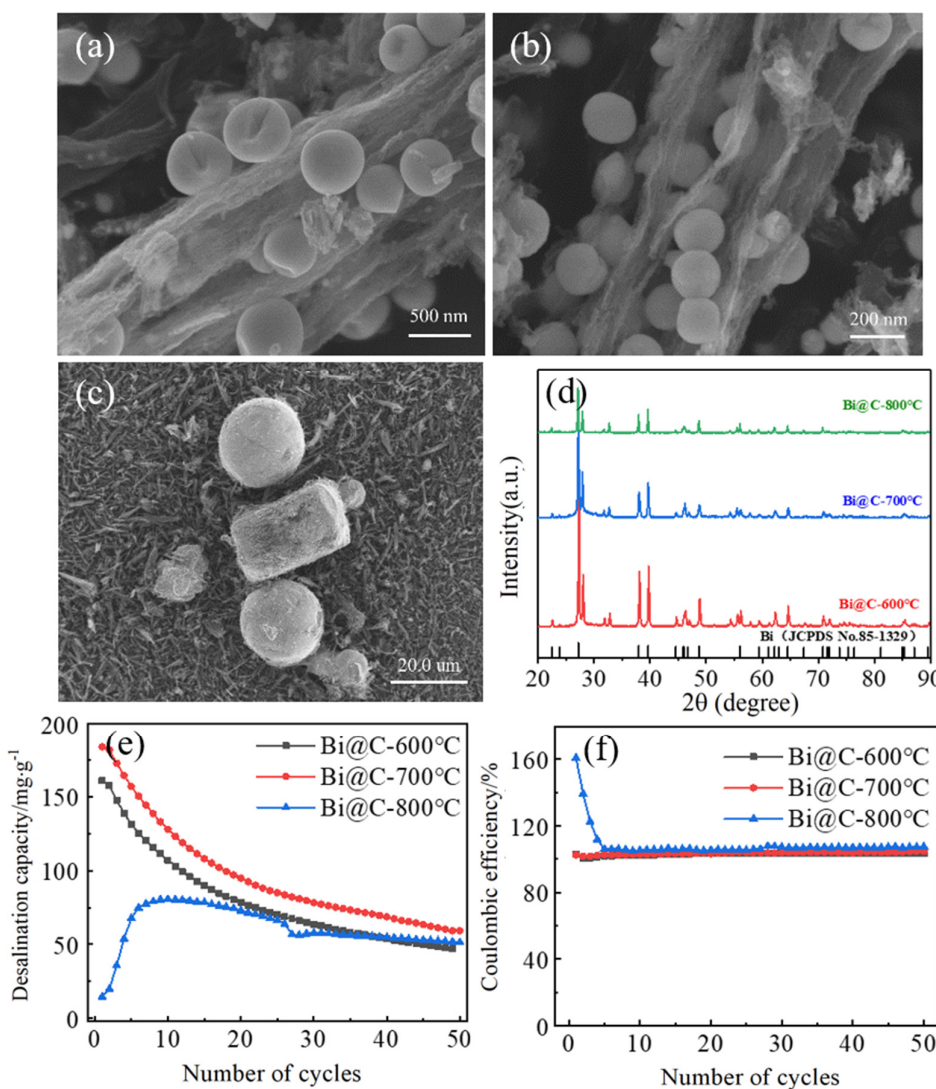


**Figure 1.** SEM images of (a) Bi@C-600 °C, (b) Bi@C-700 °C, and (c) Bi@C-800 °C; comparison of (d) XRD, (e) desalination capacity, and (f) Coulombic efficiency of materials at different sintering temperatures.

Then, the desalination ability of the material was tested at three different temperatures. As can be seen from Figure 1e, the maximum desalination capacities for Bi@C-600 °C, Bi@C-700 °C, and Bi@C-800 °C were 160.5, 183.6, and 80.4 mg/g, respectively. Moreover, as can be seen from Figure 1f, the Coulombic efficiency of Bi@C-600 °C and Bi@C-700 °C was better than that of Bi@C-800 °C, both of which were about 103%, with a small amount of side reactions. Analyzing the reasons, it can be seen that the Bi particle size had a greater effect on the desalination capacity, while the support of the carbon skeleton was more helpful for the desalination stability. According to the above analysis, when the annealing temperature was 700 °C, the Bi@C had the best desalination performance.

### 3.1.2. Optimization of Sintering Time

The shorter the sintering time, the smaller the size of the Bi ball, but the thickness of the carbon shell will be larger, thus preventing the contact of chloride ions with the Bi metal particles. However, too long of a sintering time will also cause the Bi particles to gradually gather and increase in size, which will lead to a reduction in the desalt capacity and life of the electrode. XRD tests were performed to determine the phase composition of the material, and the results are shown in Figure S1. The main diffraction peaks of Bi@C-2 h

all corresponded to the Bi standard map, which proved that the ideal material could be successfully synthesized under the condition of a sintering time of two hours, and the heterogeneous peaks of the Bi oxide were more obvious in the material under the other sintering times, representing the incomplete thermal reduction of Bi. It can be seen from the SEM image that the Bi ball particles at Bi@C-0.5 h (Figure 2a) were spherical-concave with irregular distribution. The reason was that the annealing time was short and most of the Bi metal particles were covered in carbon shells, which could not be observed in the figure. For Bi@C-1 h (Figure 2b), the Bi metal particles coated in the carbon shell could be seen faintly. The size distribution of the Bi metal particles was wide, with the minimum visible particle size being 50 nm and the maximum particle size being 210 nm. However, most of the Bi particles were still coated and the particle size could not be determined. The carbon skeleton of Bi@C-2 h (Figure 2c) was pod-like and covered with Bi spherical particles. The particles were round, the carbon skeleton was thin, and the coated Bi particles were clearly visible. The particle size ranged from 50 to 180 nm, with an average particle size of 120 nm. On the other hand, the Bi spheres in Bi@C-4 h (Figure 2d) were basically exposed on the surface of the carbon skeleton, and the particle size mainly ranged from 70 to 220 nm, with an average particle size of 148 nm. At the same temperature and sintering time of 2 h, the particle size of the product was smaller and more uniform.

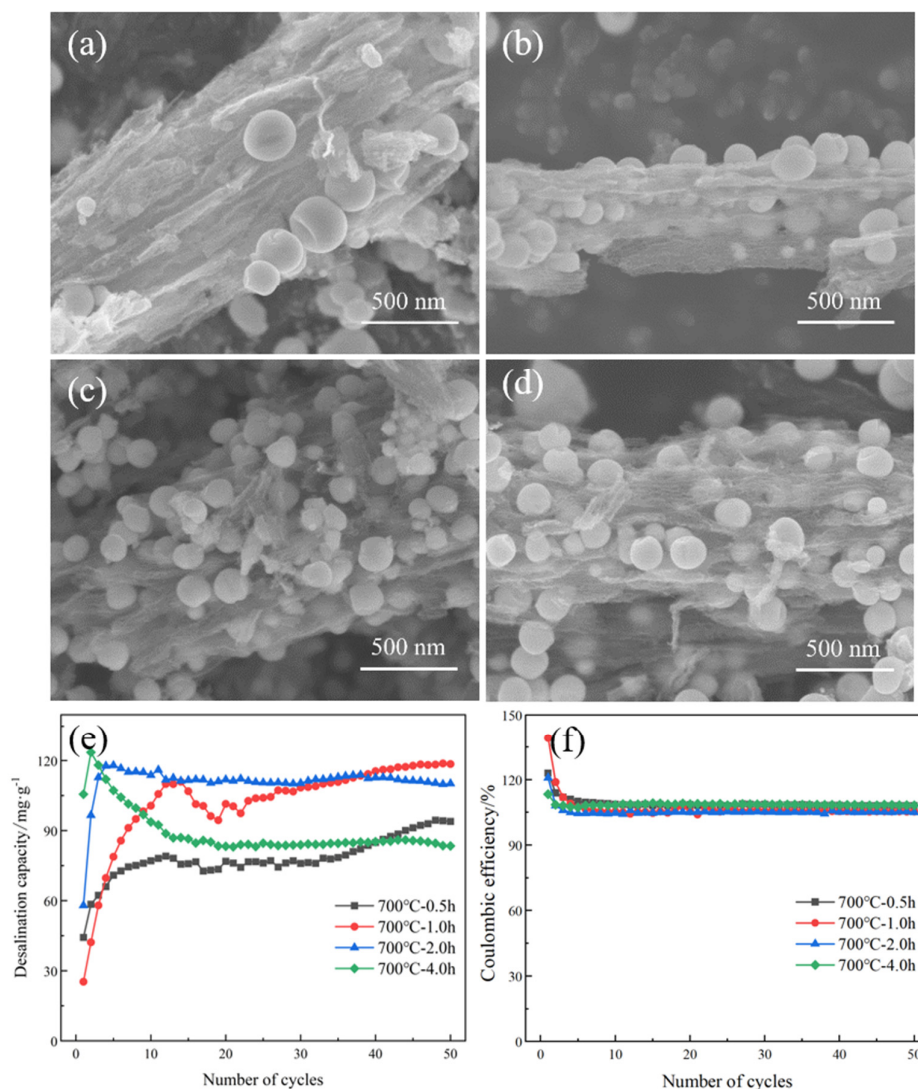


**Figure 2.** SEM images of (a) Bi@C-0.5 h, (b) Bi@C-1.0 h, (c) Bi@C-2.0 h, and (d) Bi@C-4.0 h; comparison of (e) desalination capacity and (f) Coulombic efficiency of materials at different sintering times.

The materials under different annealing times were compared with a constant-current charge–discharge test. It can be seen from Figure 2e,f that all the materials had an activation phenomenon at the initial stage. When the annealing time was shorter, the carbon shell was thicker. Most of the Bi was covered in the carbon shell, and the activation energy required was higher. When the annealing time was 2 h, Bi@C-2 h reached the maximum desalination capacity in the fourth cycle, that is, 117.7 mg/g, and basically maintained a stable desalination capacity in the 50 cycles. The capacity after the cycle was 110.1 mg/g, and the capacity retention rate was as high as 93.5%. When the reaction became stable, the Coulombic efficiency of each material was stable at 105% to 108%. Therefore, the Bi@C-2 h material with an annealing time of 2 h had the best desalination performance.

### 3.2. Characterization of Bismuth Carbon Materials Derived from MOFs

After optimizing the synthesis protocol, Bi@C-2 h was selected as the chloride-storage electrode material in this study. As can be seen from Figure 3a, Bi@C-2 h was composed of Bi, C, N, and O elements, all of which were evenly distributed, indicating that the synthesized material had uniform composition. The distributed oxygen element was the oxygen in the Bi oxide that was not completely reduced during the synthesis process, and the oxygen in the Bi oxide synthesized during the oxidation reaction with air during the storage process. The main components of the material were Bi and carbon elements, in which Bi elements accounted for 28.13% of the total atoms, and carbon elements accounted for 52.72% of the total atoms. Similarly, XPS tests also confirmed the presence of Bi, C, O, and N in the material. As can be seen from the high-resolution XPS map of Bi 4f in Figure 3c, the peaks of binding energy at 159.2 and 164.5 eV corresponded to Bi 4f<sub>7/2</sub> and Bi 4f<sub>5/2</sub>, respectively, so the surface of the Bi had been oxidized by air into a layer of Bi oxide. Through the analysis of the O 1 s diagram in Figure 3e, it can be found that the Bi formed a Bi-O-C (530.2 eV) bonding mode with O and C [23]. When nitrogen was added into the carbon structure, because the electronegativity of nitrogen atoms is large, the conductivity of the material could be increased, and the electrochemical activity could be improved. When the doping content of pyridine nitrogen is higher, it is more conducive to promoting ion diffusion. It should be noted that the XPS profiles of pyridine nitrogen, graphite nitrogen, and nitrogen oxide could be obtained from the material, corresponding to the binding energies of 398.5, 401.1, and 405.4 eV, as shown in Figure 3f.

In the process of desalination, the specific surface area of the material affected the adsorption of the water molecules and salt ions. The specific surface area of Bi@C-2 h was determined with nitrogen adsorption and desorption test. As can be seen from Figure 4a, the adsorption and desorption curves are shown as a type II isotherm, and the specific surface area was calculated to be 90.400 m<sup>2</sup>/g. The pore size distribution was analyzed using the BJH model (Figure 4b), and the pore size of the material was mainly distributed between 2 and 22 nm, with an average pore size of 7.084 nm. The data showed that the material had a large specific surface area, which meant that the Bi carbon material generated by MOF annealing had a porous property, which was conducive to increasing the area of the electrochemical reaction, thereby increasing the active site of the reaction and improving the electrochemical performance.

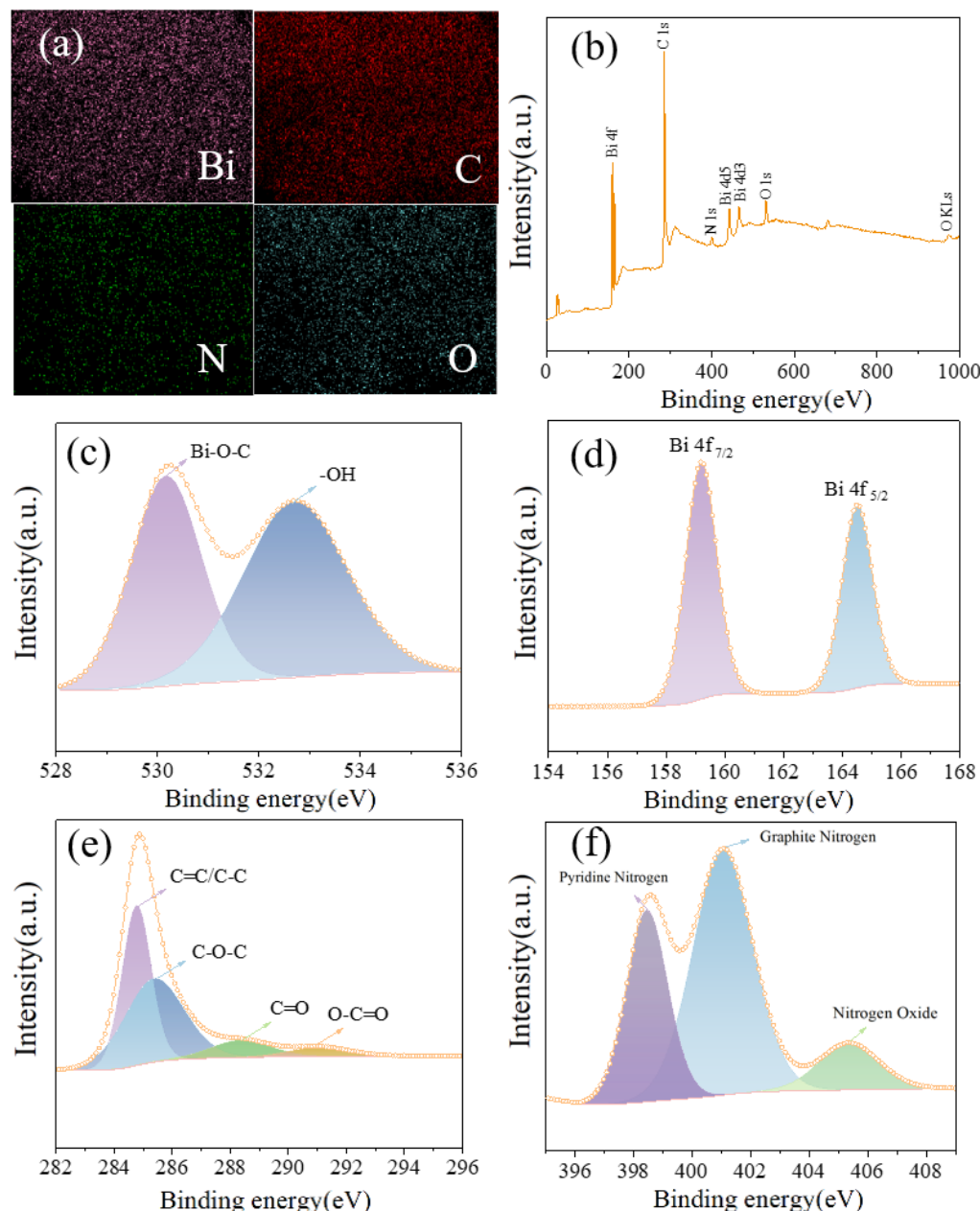


**Figure 3.** (a) EDX elemental mapping and (b) XPS spectra of Bi@C-2 h; (c) high-resolution Bi 4f XPS spectra of Bi@C-2 h; high-resolution 1 s XPS spectra of (d) C, (e) O, and (f) N of Bi@C-2 h.

The composition of Bi@C-2 h was analyzed with thermogravimetric analysis. The result is shown in Figure 4c. Compared with Bi nanoparticles, the results showed that the mass loss of Bi@C-2 h was about 2% before 157 °C, which was due to the volatilization of adsorbed water molecules in the material, and then the mass increased due to Bi oxidation. When the temperature exceeded 290 °C, the carbon in the Bi@C-2 h material was pyrolytic. The final mass ratio of the material was 87.74% of the original, and the final material was mainly Bi oxide ( $\text{Bi}_2\text{O}_3$ ). After conversion, the mass ratio of Bi in the Bi carbon material was about 78.7%. In contrast, due to the presence of a small amount of Bi oxide impurities, the mass ratio of Bi obtained under the same conditions was 96.5%.

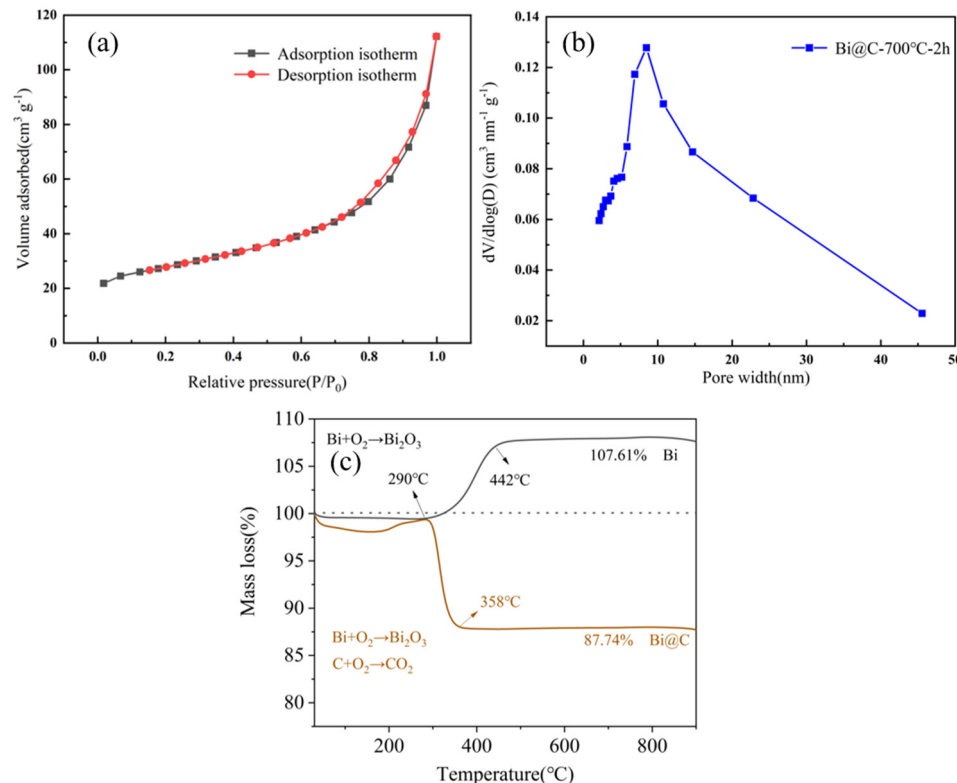


**Figure 4.** (a) Nitrogen absorption and desorption curves of Bi@C-2 h; (b) differential pore size distribution curve of Bi@C-2 h; (c) thermogravimetric curve of Bi@C-2 h and Bi metal.

### 3.3. Electrochemical Performance Test

The cyclic voltammetry of the Bi-carbon electrode was measured at different scanning rates. As shown in Figure 5a, there was a pair of symmetric oxidation peak and reduction peak in the CV diagram; the peak shape was uniform, and the ratio of peak currents between the cathode and anode peaks was close to 1, which had good reversibility. In addition, the relationship between the peak current, the scanning rate, and half of the scanning rate was linear, so the reaction between the electrode and chloride ion was controlled by diffusion and surface adsorption.

It can be observed (Figure 5b) that at a low current density of 100 mA/g, the Coulombic efficiency was as high as 160% to 210%. After the current density increased, the material had the opportunity to contact more electrons, thus improving the electron utilization rate of the material, and the side reaction of water was relatively weaker. In the later stage, the change of current density had no obvious effect on the demineralization capacity of the material, and the demineralization capacity was basically maintained at 96 mg/g. Therefore, due to the excellent electrical conductivity of Bi@C, under the condition of changing the current density, it had little effect on the desalination performance of the Bi carbon electrode, but it would change the strength relationship between the side and main reactions.

It can be seen from Figure 5c that when the electrolyte concentration was lower than 0.05 mol/L, the initial capacity of the electrode material was very low during the desalination cycle. When the electrolyte concentration was higher than 2 mol/L, the initial capacity of the electrode material was high, but after 20 cycles of charge and discharge, the capacity decayed to almost 0. When the electrolyte concentration was between 0.1 and 1 mol/L, the maximum desalination capacity of the Bi-carbon electrode material increased with the increase in the electrolyte concentration and stabilized at 90 to 120 mg/g after 50 cycles. When the electrolyte concentration was 0.2–0.6 mol/L, the electrode material exhibited the best cycling performance. As can be seen from Figure 5d, with the stability of the reaction, the Coulombic efficiency of the Bi@C at different concentrations was finally around 105%, with a low side reaction degree and high energy utilization rate.

The Bi@C was tested for 200 cycles. As can be seen from Figure 5e, the highest salt removal content of Bi@C-2 was 141.9 mg/g, which decayed to 95 mg/g after 30 cycles, and then stabilized between 86 and 95 mg/g in the subsequent cycles. Therefore, the structure of the material remained stable during the reaction.

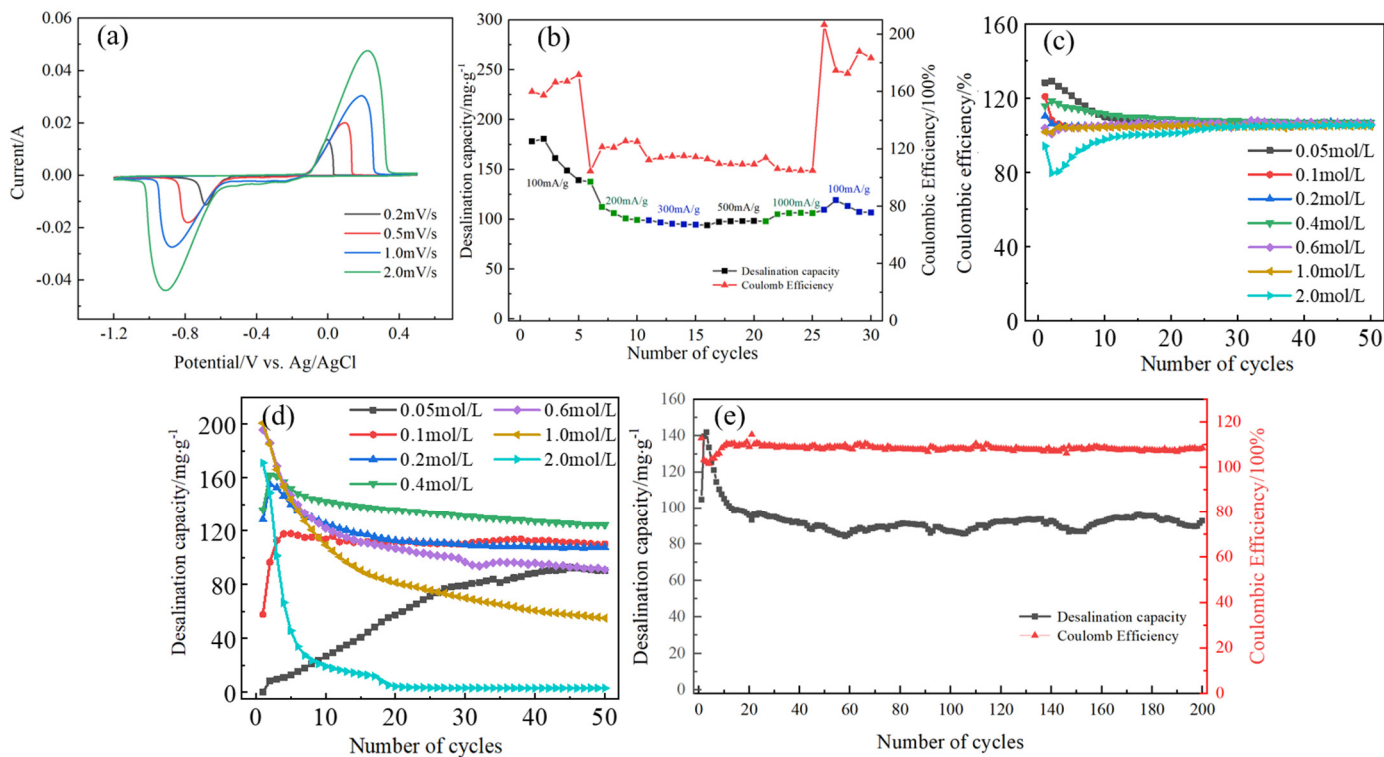
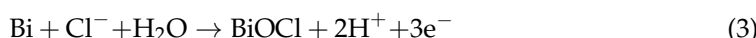


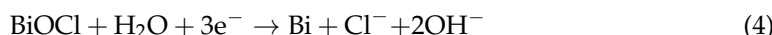
**Figure 5.** (a) Cyclic voltammetry curve and (b) rate performance of Bi@C-2 h; comparison of (c) desalination capacity and (d) Coulombic efficiency at different concentrations; (e) long cycle performance of Bi@C-2 h.

### 3.4. Analysis of Desalination Mechanism

The main reactions of Bi@C during the known chloride-storage process are:



During the chlorination process, the main reactions of Bi@C are:



It is observed that in the Bi@C-2 h electrode plate (Figure 6a–c), before the desalination cycle, Bi metal particles are mainly confined to the electrode plate by the carbon skeleton and made conductive by the carbon skeleton. After five cycles, it could be seen that a small amount of Bi metal particles were detached from the carbon skeleton structure, which was the main reason for the degradation of the Bi carbon electrode's desalination capacity. After 50 cycles, the carbon skeleton remained stable, in which bound Bi metal particles steadily contributed to capacity. And as can be seen from Figure S3, when the first chlorine storage was performed on the bare Bi electrode, the surface appeared fragmented due to the occurrence of a large volume expansion leading to the pulverization of the material. However, the interior of the Bi particles did not come into contact with the chloride ions and therefore did not participate in the reaction. After 5 and 50 cycles of desalination, only the surface of the Bi particles appeared to be detached, and the Bi particles remained in a granular form without large-scale fractures.

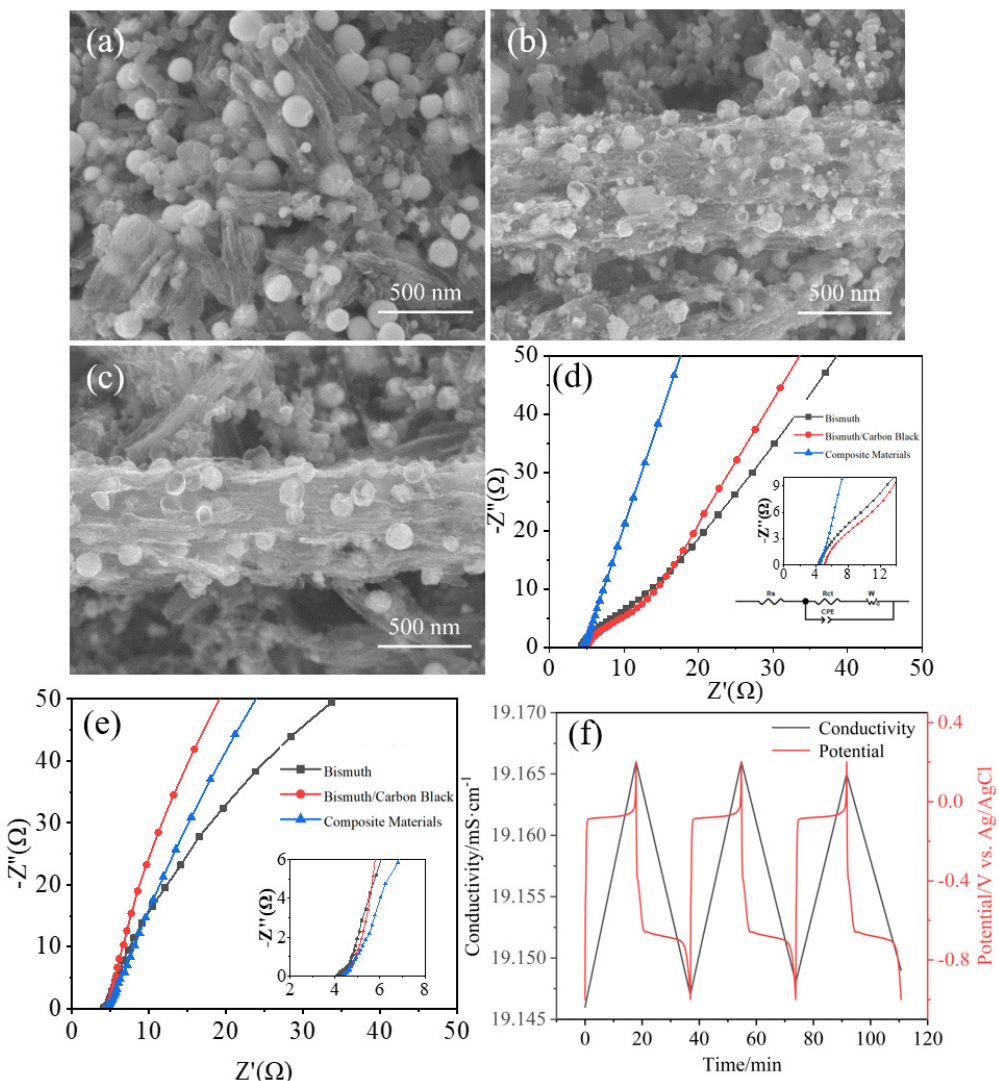


**Figure 6.** SEM images of Bi@C-2 h electrode (a) before reaction, (b) after fifth chlorination, and (c) after 50 desalination/salination cycles; electrochemical impedance spectra of the electrode (d) before reaction and (e) after 50 cycles; (f) changes in electrical conductivity during charging and discharging.

In conclusion, most of the Bi particles could be fixed on the electrode sheet due to the protection of the carbon skeleton of the Bi@C, and the porous carbon structure and small particle size of the Bi particles also promoted the contact and reaction between the ions and the electrode sheet. On the other hand, the bare Bi electrode without any modification had poor electrical conductivity and a large particle size, and the ions and electrons could not penetrate deep into the Bi spheres to react, resulting in a small percentage of functional Bi and a capacity far below the theoretical capacity.

An impedance analysis was performed for Bi@C-2 h. The unmodified bare Bi electrode was compared with the Bi-carbon black electrode doped with 10% carbon black by mass ratio. Figure 6d shows the impedance diagram before the reaction of the three electrodes. The electrode reaction was controlled by electrochemistry and concentration polarization. It could be observed that the semicircle of the high frequency region and the intercept value of the X-axis were basically the same, that is, the solution resistance was close. The semicircle diameter of Bi@C was smaller than that of the bare Bi electrode and Bi-carbon black electrode, which meant that the ion charge transfer resistance of the Bi@C electrode was smaller than that of the bare Bi electrode and Bi-carbon black electrode. The slope of the low frequency Bi@C electrode was also greater than that of the bare Bi electrode and

Bi-carbon black, that is, the impedance value of chloride ion diffusion at the interface of the Bi@C electrode system was smaller. After 50 cycles of charge and discharge (Figure 6e), the interface diffusion resistance of the Bi electrode was relatively large, and the ion charge transfer resistance of the three electrodes was close to that of the Bi@C electrode and the Bi-carbon black electrode. During the reaction, the impedance changes of various materials were compared, as shown in Figure S3. It could be found that the impedance of the Bi@C electrode remained stable during the reaction, which meant that the structure of the Bi@C was stable during the reaction, and the ionic charge transfer resistance and ionic interface diffusion resistance were better than those of the bare Bi electrode and the Bi-carbon black electrode.

The change of electrical conductivity during charge and discharge is shown in Figure 6f. The discharge process of the electrolytic cell corresponded to the conversion of Bi stored chloride into Bi oxychloride, which was consistent with the decreasing trend of the electrical conductivity of the solution. However, during the charging process of the electrolytic cell, Bi oxychloride released chloride ions and reduced to Bi, and the chloride ions in the solution increased, and the conductivity increased. Because the applied current was a constant current, the conductivity of the electrolyte also showed a linear change with the increase in time, which proved that the current input was used by the electrode chloride-storage process. Therefore, in the process of charging and discharging, the removal of chloride ions occurred in the Bi@C electrode, which led to the change in electrical conductivity.

#### 4. Conclusions

In this study, carbon-coated Bi nanocomposites (Bi@C) were prepared with the facile pyrolysis of a Bi-based MOF. The size of the synthesized Bi nanoparticles and the thickness of the carbon layer highly depended on the annealing temperature and time. The optimal sample (i.e., Bi@C-2 h) with a high desalination capacity and long cycle life was attained with annealing at 700 °C for 2 h. At the current density of 500 mA/g, the desalination capacity of the Bi@C was up to 141.9 mg/g, and the capacity retention rate was 66.9% after 200 cycles. In addition, the Bi@C could work at a wide range of NaCl concentrations from 0.05 to 2 mol/L, and the optimal working concentration was 0.2 to 0.6 mol/L. According to the mechanism analysis of salt removal, it could be seen that the Bi@C maintained good stability in the reaction process thanks to the stable carbon skeleton structure, which reserved space for the volume expansion of Bi during the chloride-storage process. In addition, the porous carbon skeleton provided electron and ion channels, and the impedance of the Bi@C was low. This study is of great significance for the application of chloride-storage electrode materials in the desalination system.

**Supplementary Materials:** The following supporting information can be downloaded at: <https://www.mdpi.com/article/10.3390/batteries10010035/s1>, Figure S1: XRD pattern of materials at different annealing times; Figure S2: Charge and discharge curves at different current densities; Figure S3: SEM image of demineralization process of Bi@C-2 h electrode and bare bismuth electrode. Bi@C-2 h electrode: (a1) before reaction; (b1) After the first storage of chlorine; (c1) After the first chlorination; (d1) After the fifth chlorination; (e1) After the 50th chlorination; Bare bismuth electrode: (a2) before reaction; (b2) After the first storage of chlorine; (c2) after the first discharge of chlorine; (d2) After the fifth chlorination; (e2) After the 50th chlorination; Figure S4: Impedance changes during the reaction of (a) bare bismuth electrode, (b) bismuth-carbon black electrode; (c) Bi@C electrode; Table S1: Comparison of desalination capacity of Bi@C based DB with various carbon, pseudocapacitor and Faraday electrode materials reported in the literature. References [29–37] are cited in the supplementary materials.

**Author Contributions:** Writing—original draft, X.D., Y.W. and Q.Z.; Project administration, Funding acquisition, Data curation, C.L. All authors have read and agreed to the published version of the manuscript.

**Funding:** This work was supported by the National Natural Science Foundation of China (Grant No. 52100084).

**Data Availability Statement:** The raw data supporting the conclusions of this article will be made available by the authors on request.

**Acknowledgments:** The authors would like to express their gratitude to Wenhui Wang at the Harbin Institute of Technology, Shenzhen, for his support and helpful discussions.

**Conflicts of Interest:** The authors declare no conflict of interest.

## References

- Barnett, T.P.; Adam, J.C.; Lettenmaier, D.P. Potential Impacts of a Warming Climate on Water Availability in Snow-Dominated Regions. *Nature* **2005**, *438*, 303–309. [[CrossRef](#)] [[PubMed](#)]
- Dolan, F.; Lamontagne, J.; Link, R.; Hejazi, M.; Reed, P.; Edmonds, J. Evaluating the Economic Impact of Water Scarcity in a Changing World. *Nat. Commun.* **2021**, *12*, 1915. [[CrossRef](#)] [[PubMed](#)]
- Xu, D.; Wang, W.; Zhu, M.; Li, C. Recent Advances in Desalination Battery: An Initial Review. *ACS Appl. Mater. Interfaces* **2020**, *12*, 57671–57685. [[CrossRef](#)]
- Qasim, M.; Badrelzaman, M.; Darwish, N.N.; Darwish, N.A.; Hilal, N. Reverse Osmosis Desalination: A State-of-the-Art Review. *Desalination* **2019**, *459*, 59–104. [[CrossRef](#)]
- Al-Othman, A.; Tawalbeh, M.; El Haj Assad, M.; Alkayyali, T.; Eisa, A. Novel Multi-Stage Flash (MSF) Desalination Plant Driven by Parabolic Trough Collectors and a Solar Pond: A Simulation Study in UAE. *Desalination* **2018**, *443*, 237–244. [[CrossRef](#)]
- Service, R.F. Desalination Freshens Up. *Science* **2006**, *313*, 1088–1090. [[CrossRef](#)]
- Suss, M.E.; Presser, V. Water Desalination with Energy Storage Electrode Materials. *Joule* **2018**, *2*, 10–15. [[CrossRef](#)]
- Porada, S.; Zhao, R.; Van Der Wal, A.; Presser, V.; Biesheuvel, P.M. Review on the Science and Technology of Water Desalination by Capacitive Deionization. *Prog. Mater. Sci.* **2013**, *58*, 1388–1442. [[CrossRef](#)]
- Wang, G.; Yan, T.; Zhang, J.; Shi, L.; Zhang, D. Trace-Fe-Enhanced Capacitive Deionization of Saline Water by Boosting Electron Transfer of Electro-Adsorption Sites. *Environ. Sci. Technol.* **2020**, *54*, 8411–8419. [[CrossRef](#)]
- Wang, H.; Wei, D.; Gang, H.; He, Y.; Deng, H.; Hou, L.; Shi, Y.; Wang, S.; Yang, W.; Zhang, L. Hierarchical Porous Carbon from the Synergistic “Pore-on-Pore” Strategy for Efficient Capacitive Deionization. *ACS Sustain. Chem. Eng.* **2020**, *8*, 1129–1136. [[CrossRef](#)]
- Zhang, L.; Zhang, M.; Liu, G.; Jin, W.; Li, X. Fungal Cell Wall-Graphene Oxide Microcomposite Membrane for Organic Solvent Nanofiltration. *Adv. Funct. Mater.* **2021**, *31*, 2100110. [[CrossRef](#)]
- Doornbusch, G.J.; Dykstra, J.E.; Biesheuvel, P.M.; Suss, M.E. Fluidized Bed Electrodes with High Carbon Loading for Water Desalination by Capacitive Deionization. *J. Mater. Chem. A* **2016**, *4*, 3642–3647. [[CrossRef](#)]
- Suss, M.E.; Porada, S.; Sun, X.; Biesheuvel, P.M.; Yoon, J.; Presser, V. Water Desalination via Capacitive Deionization: What Is It and What Can We Expect from It? *Energy Environ. Sci.* **2015**, *8*, 2296–2319. [[CrossRef](#)]
- Liu, X.; Shanbhag, S.; Bartholomew, T.V.; Whitacre, J.F.; Mauter, M.S. Cost Comparison of Capacitive Deionization and Reverse Osmosis for Brackish Water Desalination. *ACS EST Eng.* **2021**, *1*, 261–273. [[CrossRef](#)]
- Liu, Y.; Wang, K.; Xu, X.; Eid, K.; Abdullah, A.M.; Pan, L.; Yamauchi, Y. Recent Advances in Faradic Electrochemical Deionization: System Architectures versus Electrode Materials. *ACS Nano* **2021**, *15*, 13924–13942. [[CrossRef](#)]
- Chen, F.; Huang, Y.; Kong, D.; Ding, M.; Huang, S.; Yang, H.Y. NaTi<sub>2</sub>(PO<sub>4</sub>)<sub>3</sub>-Ag Electrodes Based Desalination Battery and Energy Recovery. *FlatChem* **2018**, *8*, 9–16. [[CrossRef](#)]
- Xiong, Y.; Yu, F.; Ma, J. Research Progress in Chlorine Ion Removal Electrodes for Desalination by Capacitive Deionization. *ACTA Phys.-Chim. Sin.* **2021**, *38*, 20–31. [[CrossRef](#)]
- Ahn, J.; Lee, J.; Kim, S.; Kim, C.; Lee, J.; Biesheuvel, P.M.; Yoon, J. High Performance Electrochemical Saline Water Desalination Using Silver and Silver-Chloride Electrodes. *Desalination* **2020**, *476*, 114216. [[CrossRef](#)]
- He, Y.; Huang, L.; Zhao, Y.; Yang, W.; Hao, T.; Wu, B.; Deng, H.; Wei, D.; Wang, H.; Luo, J. A Newly Synthesized Highly Stable Ag/N-Carbon Electrode for Enhanced Desalination by Capacitive Deionization. *Environ. Sci. Nano* **2020**, *7*, 3007–3019. [[CrossRef](#)]
- Liang, M.; Wang, L.; Presser, V.; Dai, X.; Yu, F.; Ma, J. Combining Battery-Type and Pseudocapacitive Charge Storage in Ag/Ti<sub>3</sub>C<sub>2</sub>T<sub>x</sub> MXene Electrode for Capturing Chloride Ions with High Capacitance and Fast Ion Transport. *Adv. Sci.* **2020**, *7*, 2000621. [[CrossRef](#)]
- Yue, Z.; Ma, Y.; Zhang, J.; Li, H. Pseudo-Capacitive Behavior Induced Dual-Ion Hybrid Deionization System Based on Ag@rGO||Na<sub>1.1</sub>V<sub>3</sub>O<sub>7.9</sub>@rGO. *J. Mater. Chem. A* **2019**, *7*, 16892–16901. [[CrossRef](#)]
- Xu, D.; Wang, W.; Zhu, M.; Li, C. Carbon Nanotubes Composite Embedded with Silver Nanoparticles as Chloride Storage Electrode for High-Capacity Desalination Batteries. *Sep. Purif. Technol.* **2022**, *299*, 121731. [[CrossRef](#)]
- Nam, D.-H.; Choi, K.-S. Bismuth as a New Chloride-Storage Electrode Enabling the Construction of a Practical High Capacity Desalination Battery. *J. Am. Chem. Soc.* **2017**, *139*, 11055–11063. [[CrossRef](#)] [[PubMed](#)]
- Chen, F.; Huang, Y.; Guo, L.; Sun, L.; Wang, Y.; Yang, H.Y. Dual-ions electrochemical deionization: A desalination generator. *Energ. Environ. Sci.* **2017**, *10*, 2081–2089. [[CrossRef](#)]
- Chang, J.; Duan, F.; Su, C.; Li, Y.; Cao, H. Removal of Chloride Ions Using a Bismuth Electrode in Capacitive Deionization (CDI). *Environ. Sci. Water Res. Technol.* **2020**, *6*, 373–382. [[CrossRef](#)]
- Nam, D.-H.; Lumley, M.A.; Choi, K.-S. A Desalination Battery Combining Cu<sub>3</sub>[Fe(CN)<sub>6</sub>]<sub>2</sub> as a Na-Storage Electrode and Bi as a Cl-Storage Electrode Enabling Membrane-Free Desalination. *Chem. Mater.* **2019**, *31*, 1460–1468. [[CrossRef](#)]

27. Liu, Y.; Gao, X.; Wang, Z.; Wang, K.; Dou, X.; Zhu, H.; Yuan, X.; Pan, L. Controlled Synthesis of Bismuth Oxychloride-Carbon Nanofiber Hybrid Materials as Highly Efficient Electrodes for Rocking-Chair Capacitive Deionization. *Chem. Eng. J.* **2021**, *403*, 126326. [[CrossRef](#)]
28. Nam, D.-H.; Lumley, M.A.; Choi, K.-S. A Seawater Battery with Desalination Capabilities Enabling a Dual-Purpose Aqueous Energy Storage System. *Energy Storage Mater.* **2021**, *37*, 556–566. [[CrossRef](#)]
29. Wang, M.; Xu, X.T.; Liu, Y.; Li, Y.J.; Lu, T.; Pan, L.K. From metal-organic frameworks to porous carbons: A promising strategy to prepare high-performance electrode materials for capacitive deionization. *Carbon* **2016**, *108*, 433–439. [[CrossRef](#)]
30. Kim, T.; Yoon, J. CDI ragone plot as a functional tool to evaluate desalination performance in capacitive deionization. RSC advances. *RSC Adv.* **2015**, *5*, 1456–1461. [[CrossRef](#)]
31. Kim, S.; Lee, J.; Kim, C.; Yoon, J.  $\text{Na}_2\text{FeP}_2\text{O}_7$  as a novel material for hybrid capacitive deionization. *Electrochim. Acta* **2016**, *203*, 265–271. [[CrossRef](#)]
32. Cao, J.; Wang, Y.; Wang, L.; Yu, F.; Ma, J.  $\text{Na}_3\text{V}_2(\text{PO}_4)_3@\text{C}$  as faradaic electrodes in capacitive deionization for high-performance desalination. *Nano Lett.* **2019**, *19*, 823–828. [[CrossRef](#)] [[PubMed](#)]
33. Li, Y.; Ding, Z.; Li, J.; Li, J.; Lu, T.; Pan, L. Highly efficient and stable desalination via novel hybrid capacitive deionization with redox-active polyimide cathode. *Desalination* **2019**, *469*, 114098. [[CrossRef](#)]
34. Guo, Z.; Ma, Y.; Dong, X.; Hou, M.; Wang, Y.; Xia, Y. Integrating Desalination and Energy Storage using a Saltwater-based Hybrid Sodium-ion Supercapacitor. *ChemSusChem* **2018**, *11*, 1741–1745. [[CrossRef](#)]
35. Lee, J.; Jo, K.; Lee, J.; Hong, S.P.; Kim, S.; Yoon, J. Rocking-chair capacitive deionization for continuous brackish water desalination. *ACS Sustain. Chem. Eng.* **2018**, *6*, 10815–10822. [[CrossRef](#)]
36. Huang, Y.; Chen, F.; Guo, L.; Zhang, J.; Chen, T.; Yang, H.Y. Low energy consumption dual-ion electrochemical deionization system using  $\text{NaTi}_2(\text{PO}_4)_3$ -AgNPs electrodes. *Desalination* **2018**, *451*, 241–247. [[CrossRef](#)]
37. Zhao, W.; Guo, L.; Ding, M.; Huang, Y.; Yang, H.Y. Ultrahigh-desalination-capacity dual-ion electrochemical deionization device based on  $\text{Na}_3\text{V}_2(\text{PO}_4)_3@\text{C}-\text{AgCl}$  electrodes. *ACS Appl. Mater. Inter.* **2018**, *10*, 40540–40548. [[CrossRef](#)]

**Disclaimer/Publisher’s Note:** The statements, opinions and data contained in all publications are solely those of the individual author(s) and contributor(s) and not of MDPI and/or the editor(s). MDPI and/or the editor(s) disclaim responsibility for any injury to people or property resulting from any ideas, methods, instructions or products referred to in the content.